Volume 18
Number 8
26 February 2026
Pages 3957-4474

Nanoscale

rsc.li/nanoscale

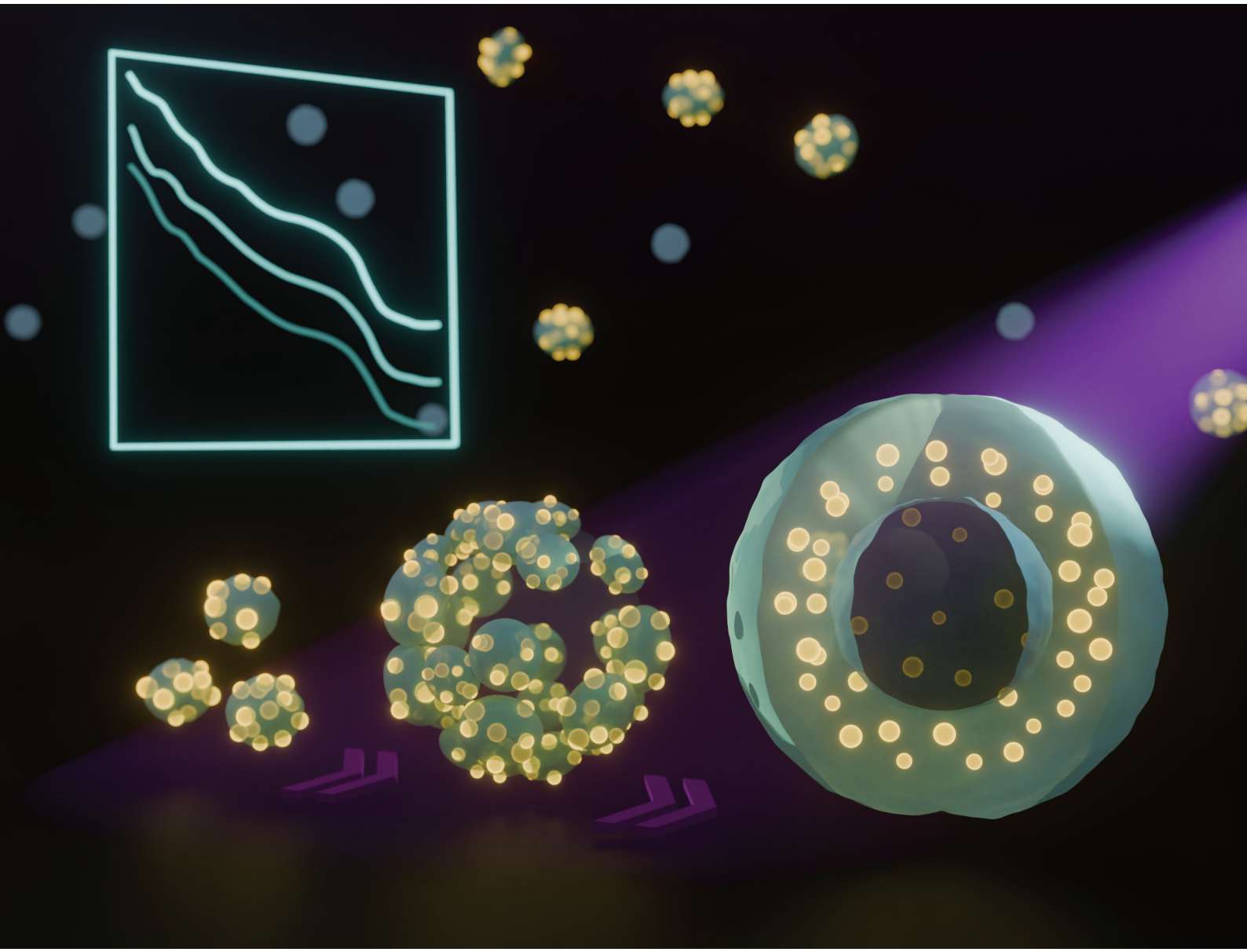

ISSN 2040-3372

ROYAL SOCIETY OF CHEMISTRY

PAPER
Hsiung-Lin Tu *et al.*
One-step photochemical synthesis of gold–polymer nanohybrids with engineered morphologies and catalytic activity

NCNST

Nanoscale

PAPER

View Article Online
View Journal | View Issue

Cite this: *Nanoscale*, 2026, **18**, 4074

One-step photochemical synthesis of gold–polymer nanohybrids with engineered morphologies and catalytic activity

Meng-Jie Wu,[a] Reynaldo Carlos Kuizon Montalbo,[a] Chun-Jen Su,[b] Orion Shih[b] and Hsiung-Lin Tu *[a,c]

Received 28th October 2025,
Accepted 12th January 2026

DOI: 10.1039/d5nr04546k

rsc.li/nanoscale

Thermoresponsive gold–polymer nanohybrids are promising functional materials, but their synthesis and structural control often require complex multistep processes. Herein, we report a one-step photochemical synthesis that enables the rapid formation of thermoresponsive hybrid nanogels *via* simultaneous polymerization, crosslinking, and reduction within 10 minutes. The key strength of this approach lies in its structural versatility and control. By tuning the reagent concentration and temperature, nanogels with distinct morphologies and internal architectures were obtained. Notably, this single-step method enables the direct formation of both conventional solid nanogels and sophisticated hollow spherical structures where gold nanoparticles are embedded within the thermoresponsive polymer shell. The formation mechanism of these hybrid hollow structures was systematically investigated by electron microscopy and small-angle X-ray scattering analyses for samples collected at various irradiation times. Furthermore, the thermoresponsive catalytic activity of the resulting nanogels was demonstrated *via* the reduction of 4-nitrophenol. This highlights how the readily adjustable internal structure and composition directly translate to functional properties, confirming this facile strategy as a promising route for designing hybrid nanomaterials with tailored structural complexity and function.

Introduction

Stimuli-responsive nanocomposites that integrate inorganic nanoparticles with polymers have emerged as a powerful class of smart materials owing to their versatile properties and broad applications in fields such as biomedicine, sensing, and catalysis.[1–4] Among inorganic nanomaterials, gold nanoparticles (AuNPs) have attracted attention because of their unique optical, electrical, and catalytic properties, which can be tailored by controlling the particle size and morphology.[5,6] However, their performance in aqueous environments is often compromised by a strong tendency to aggregate, reducing stability and limiting practical utility. Combination with polymers has therefore been widely employed to enhance colloidal dispersion. Beyond stabilization, stimuli-responsive polymers provide dynamic regulation by undergoing reversible structural changes in response to external stimuli such as pH or temperature.[7–10] These transitions can be leveraged to modulate interparticle spacing and local microenvironments, thereby influencing the collective properties of the resulting nanoparticles. By combining the properties of both AuNPs and responsive polymers, such nanohybrids exhibit tunable functionality and broad potential for application across diverse fields.

Indeed, several strategies have been developed to synthesize stimuli-responsive Au–polymer nanohybrids, which can be categorized according to how the two components are combined. In one approach, AuNPs and polymers are prepared separately and subsequently integrated together *via* either non-covalent interactions or covalent linkages.[11–13] Another strategy involves carrying out polymerization in the presence of preformed AuNPs, for example, by growing polymer chains or networks from anchoring groups on the nanoparticle surface.[14] A third route relies on the *in situ* reduction of gold precursors within polymeric structures, leading to the direct formation of AuNPs embedded within polymer networks.[15,16] While these methods have enabled the preparation of diverse Au–polymer hybrids, their syntheses are often accompanied by multi-step synthesis with tedious purification steps.

To overcome these drawbacks, single-step approaches for synthesizing both AuNPs and polymers simultaneously have been developed.[17] Nevertheless, achieving a one-step synthesis of Au–polymer nanocomposites with controllable mor-

[a]*Institute of Chemistry, Academia Sinica, 28 Academia Road, Section 2, Nankang, Taipei 115201, Taiwan. E-mail: hltu@gate.sinica.edu.tw*
[b]*National Synchrotron Radiation Research Center, No. 101, Hsin-Ann Road, Hsinchu Science Park, Hsinchu 30076, Taiwan*
[c]*Genome and Systems Biology Program, Academia Sinica and National Taiwan University, Taipei 10617, Taiwan*

phologies remains a significant challenge. The reaction conditions favoring nanoparticle nucleation and growth are often incompatible with those required for polymerization, thus making the optimization of reagents and conditions difficult. To date, only very limited studies have reported successful single-step methods, and examples performed in aqueous media are particularly scarce.[18,19] Furthermore, achieving morphological control in such simplified routes is even more difficult when compared to conventional multi-step approaches. For instance, hollow structures, which are especially desirable due to their internal cavities, have so far been prepared predominantly through template-assisted strategies that require sacrificial core fabrication, polymer shell deposition, and subsequent core removal.[20–22] Although alternative approaches such as soft-templating have also been explored, they often depend on multiphase systems and remain relatively complicated.[23–25] Thus, to the best of our knowledge, a straightforward one-step strategy for synthesizing Au–polymer hybrid particles with a tunable structure has not yet been realized.

In this work, we develop a one-step photochemical strategy for the synthesis of Au–polymer hybrid nanogels, in which AuNPs and polymer networks are generated simultaneously under UV irradiation in 10 minutes. In contrast to conventional thermal initiators used for polymer micro/nanogels, this approach employs a water-soluble photoinitiator, lithium phenyl-2,4,6-trimethylbenzoylphosphinate (LAP),[26–29] which can initiate polymerization while reducing gold precursors, thereby enabling the rapid formation of AuNPs embedded within nanogels across a range of reaction temperatures. As the polymer component, thermoresponsive poly(*N*-isopropylacrylamide) (PNIPAAm) was chosen because of its well-studied lower critical solution temperature (LCST) at around 32 °C, at which it undergoes a coil-to-globule transition in aqueous environments.[30,31] Notably, by tuning reaction conditions and temperature, this method provides access to hybrid nanogels with distinct morphologies, including conventional solid structures and unprecedented hollow structures, demonstrating remarkable structural control in a single step. In addition, the mechanism underlying the hollow sphere Au–PNIPAAm nanogel formation was carefully investigated by electron microscopy (EM) and small-angle X-ray scattering (SAXS). Together, they provide key insight for the hollow sphere formation. Finally, we demonstrate that the hybrid nanogels could serve as efficient, temperature-dependent catalysts for the reduction of 4-nitrophenol (4-NP), highlighting not only their functionality but also the broader potential of this rapid synthetic strategy for designing responsive hybrid nanomaterials.

Results and discussion

The facile synthesis of Au–PNIPAAm hybrid nanogels is illustrated in Scheme 1. The nanogels were synthesized *via* a single-step method, in which gold nanoparticles (AuNPs) and poly(*N*-isopropylacrylamide) (PNIPAAm) nanogels were simultaneously formed through reduction and polymerization. The reaction mixture simply contained the gold precursor (tetrachloroauric(III) acid trihydrate, $HAuCl_4{\cdot}3H_2O$), monomer (*N*-isopropylacrylamide, NIPAAm), crosslinker (*N*,*N*′-methylenebis(acrylamide), BIS), and photoinitiator (lithium phenyl-2,4,6-trimethylbenzoylphosphinate, LAP). Upon irradiation

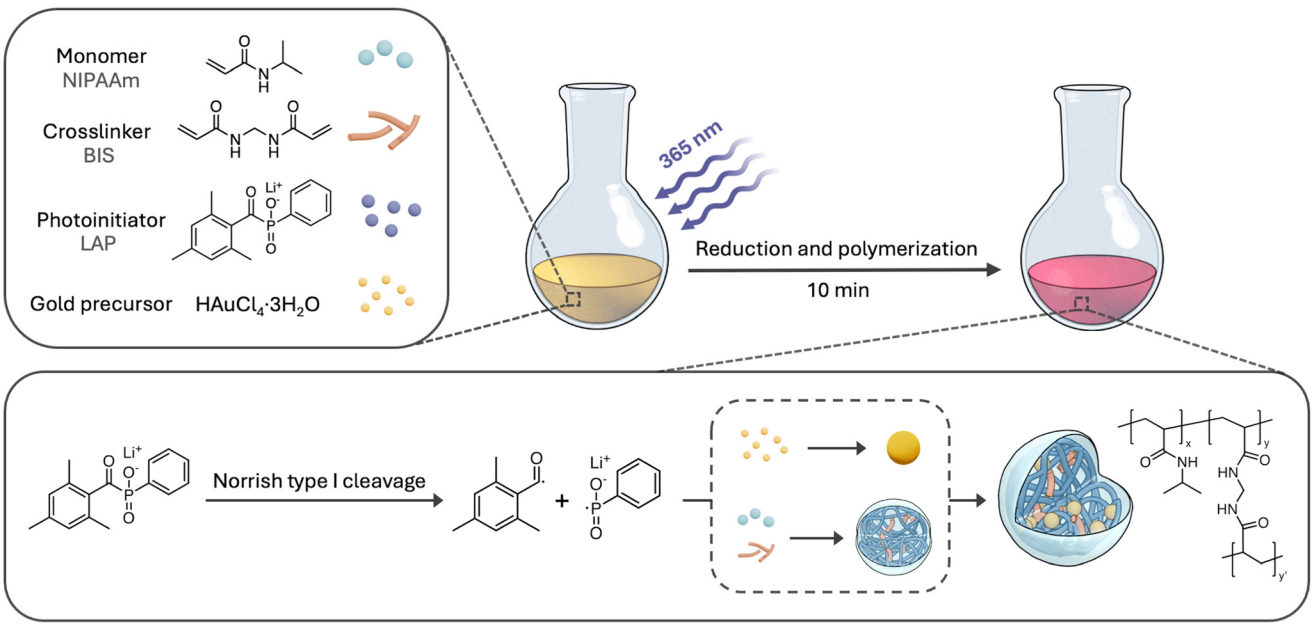

Scheme 1 Schematic of Au–PNIPAAm hybrid nanogel synthesis *via* a single-step photochemical approach. The photoinitiator LAP undergoes Norrish type I cleavage to generate radicals that drive simultaneous reduction, polymerization, and crosslinking within 10 minutes, yielding polymer nanogels with AuNPs embedded in the networks.

with 365 nm UV light, LAP undergoes Norrish type I cleavage,[26] generating radicals that simultaneously initiate free radical polymerization, crosslinking of PNIPAAm, and the reduction of Au^{3+} ions, leading to the formation of AuNPs embedded within PNIPAAm nanogels.

To investigate the effects of reagent concentration and synthesis temperature, samples were synthesized using two sets of concentrations and varying temperatures (Table 1). Prior to synthesizing under different conditions, the optimal irradiation time was determined by monitoring the size evolution of hybrid nanogels synthesized at 40 °C (H40). Hydrodynamic diameter (D_H) measurements conducted *via* dynamic light scattering (DLS) showed no significant increase after 10 minutes of UV exposure (Fig. S1). In addition, scanning electron microscopy (SEM) images at different irradiation times indicated that the particle morphology was fully developed by 10 minutes (Fig. 1A). Accordingly, an irradiation time of 10 minutes was applied to all subsequent syntheses under various conditions.

With the irradiation time fixed at 10 minutes, the low-monomer-concentration (L) series nanogels exhibited a significant change in the morphology with increasing temperature. At 25 °C (L25), particles were relatively small and not well defined compared to those prepared at higher temperatures, as evidenced by TEM and SEM images (Fig. 1B and S2A). In contrast, SEM and TEM images showed that both hybrid nanogels synthesized at 40 °C (L40) and 60 °C (L60) appeared spherical with well-defined solid structures (Fig. 1C, D, S2B, and S2C). Although the overall polymer morphologies of L40 and L60 were similar, the distribution of AuNPs differed significantly, with those in L40 located predominantly near the center of the nanogel, whereas in L60 they were uniformly distributed throughout the polymer network.

This morphological change can be attributed to the inherent thermoresponsiveness of PNIPAAm, which has a lower critical solution temperature (LCST) of 32 °C. At temperatures below LCST, PNIPAAm remains hydrated and solvated, leading to homogeneous polymerization throughout the aqueous phase.[32] Since nucleation is driven by hydrophobic interactions, such homogeneous polymerization reduces intermolecular attraction between polymer chains, resulting in the formation of more nuclei and subsequently producing higher concentrations of particles with smaller sizes. Visual observations supported this explanation, as the solutions turned dark red within approximately 30 seconds upon irradiation while remaining transparent throughout the reaction, indicating the absence of phase separation in solution. In contrast, precipitation polymerization occurs at temperatures above the LCST, during which the polymer chains undergo a coil-to-globule transition and collapse, leading to the formation of nuclei.[33] Additionally, the increased crosslinking density, developed through coalescence during polymerization, produced well-defined morphologies. Furthermore, since polymerization at 60 °C proceeded more rapidly than at 40 °C, the more uniform distribution of AuNPs in L60 may be attributed to the comparable rates of AuNP formation and polymer particle growth, which promote homogeneous incorporation of AuNPs throughout the polymer network. The observation that both L40 and L60 solutions transformed from clear to turbid within 30 s of irradiation further confirmed the occurrence of precipitation polymerization.

On the other hand, a nearly comparable temperature-dependent trend was observed for the high-monomer-concentration (H) series, but with a pronounced difference for samples synthesized at 40 °C. Specifically, Au–PNIPAAm NPs with a distinct hollow sphere morphology were successfully synthesized at H40. Structural characterization studies using TEM images revealed hollow polymer shells with AuNPs embedded in the shell and concentrated near the inner wall (Fig. 1F), which was in sharp contrast to the solid structures formed under L40 conditions. Although most hollow nanogels exhibited intact shells (Fig. S2E), a small fraction displayed surface openings (Fig. S3), further confirming the formation of hollow structures. Meanwhile, TEM and SEM images showed that the nanogels synthesized at H25 were similar to the L25 sample and appeared small and poorly defined, consistent with the previously discussed homogeneous polymerization behavior below the LCST (Fig. 1E and S2D). In addition, similar to L60, H60 also exhibited spherical, solid structures with AuNPs distributed homogeneously within the polymer network (Fig. 1G and S2F). This observation clearly suggests that distinct morphologies of hybrid nanogels can be achieved through the one-step method simply by controlling the synthesis temperature and adjusting the reagent concentration.

Table 1 Reaction conditions and characterization data of hybrid nanogels synthesized in this study

Sample	$HAuCl_4$ (mM)	NIPAAm (mM)	BIS (mM)	LAP (mM)	Temperature (°C)	Nanogel size[a] (nm)	AuNP size[b] (nm)	Au weight fraction[c] (wt%)
L25	0.5	10	0.75	12	25	75.7 ± 0.6	3.7 ± 0.8	2.8
L40	0.5	10	0.75	12	40	113.2 ± 0.2	3.7 ± 1.0	6.7
L60	0.5	10	0.75	12	60	164.3 ± 4.4	3.6 ± 0.8	4.6
H25	1	20	1.5	12	25	79.6 ± 0.3	3.0 ± 0.7	10.9
H40	1	20	1.5	12	40	238.7 ± 6.1	3.4 ± 0.7	11.3
H60	1	20	1.5	12	60	194 ± 20.6	5.2 ± 0.7	17.6

[a] Nanogel sizes are reported as hydrodynamic diameters obtained *via* DLS (n = 3) at 25 °C. [b] AuNP sizes were determined from TEM image analysis (n = 300). [c] Au weight fractions were calculated from Au concentrations measured by ICP-OES. The relative standard deviation of the ICP-OES measurements was below 1.2%.

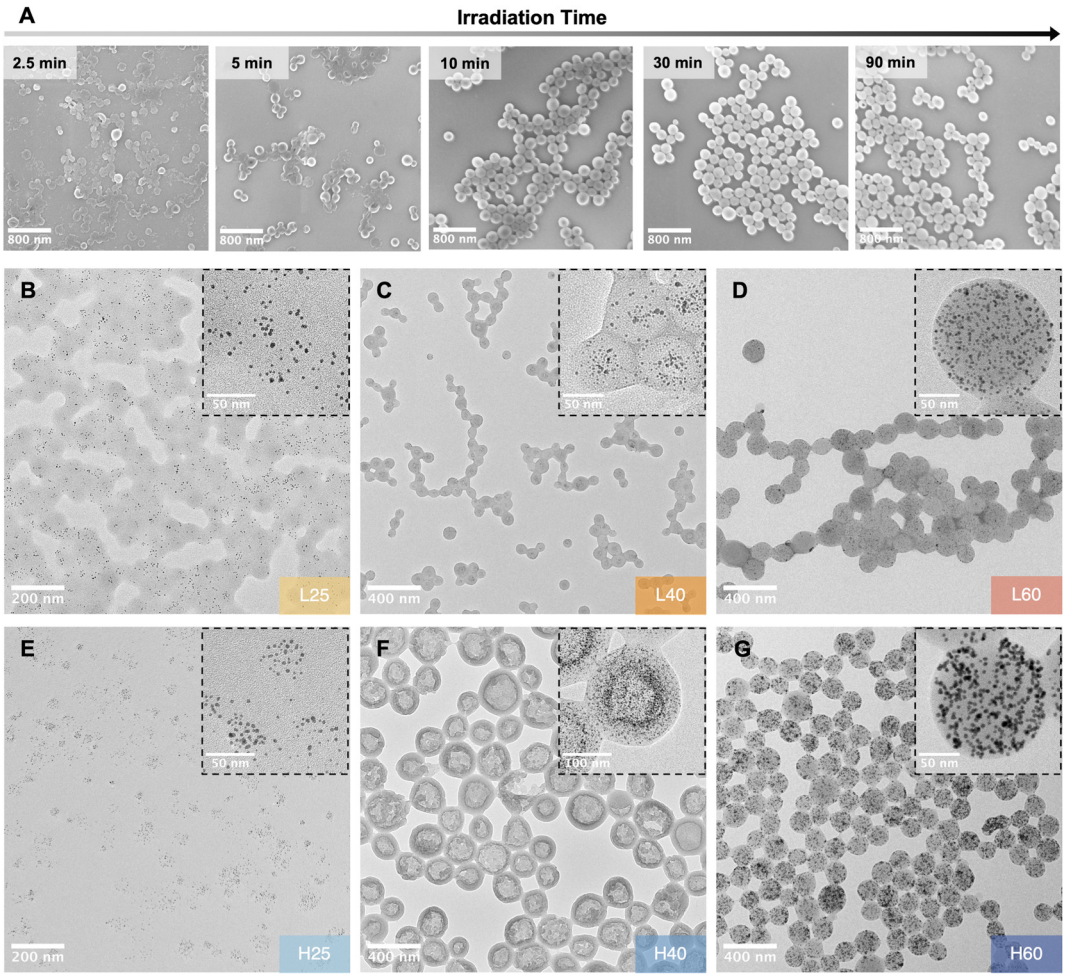

Fig. 1 (A) SEM images of H40 samples synthesized with different irradiation times. TEM images of the hybrid nanogels synthesized at different reagent concentrations and temperatures. Panels show (B) L25, (C) L40, (D) L60, (E) H25, (F) H40, and (G) H60.

To investigate the formation mechanism of the hybrid hollow nanogel (H40), samples with different irradiation times were synthesized and analyzed using SEM and TEM. As shown in Fig. 2A, most nanogels obtained after 2.5 min displayed a disk-like appearance with irregular borders, pronounced surface roughness, and AuNPs distributed throughout. At 5 min, the hollow feature became more evident, although disk-like particles were still present. In contrast, no disk-like particles were observed in the SEM images after 10 min of irradiation, and TEM revealed well-defined hollow structures. In addition, the nanogel size increased with irradiation time regardless of the morphology, indicating continued polymerization. This observation also agrees with the increased turbidity and absorbance of the as-synthesized samples (Fig. S4A and S4B).

Based on these observations, we speculated that the disk-like particles with irregular edges were precursors of hollow nanogels, likely containing a void interior with a thin Au–polymer shell. Such morphologies observed under EM may result from collapse during sample drying or under the vacuum conditions of EM. In contrast, the final hollow nanogels did not collapse because the continued growth of polymer networks reinforced the shell and stabilized the structure. To further investigate the structures in aqueous solution, cryo-TEM characterization was performed. As expected, the 2.5 min sample exhibited a spherical contour (Fig. S5A), in contrast to the amorphous edges observed in conventional EM. Although the hollow structures in the 10 min sample were less obvious in cryo-TEM (Fig. S5B), the clear contrast in morphology between the 2.5 and 10 min samples and the solid nanogels (H60) (Fig. S5C) indicates that the former are unlikely to be solid and are presumably hollow. Moreover, the 10 min sample exhibited a substantially thicker outer polymer region compared to the 2.5 min sample, indicating shell growth following the formation of precursor hollow nanogels.

Characterization using small-angle X-ray scattering (SAXS) was further performed to gain deeper insight into the hollow nanogel formation. The scattering profiles were best described using a combined Guinier + core–shell + sphere model. In this framework, the core–shell function captured the hollow nanogel architecture, the sphere term represented scattering from small Au nanoparticles, and the Guinier term accounted

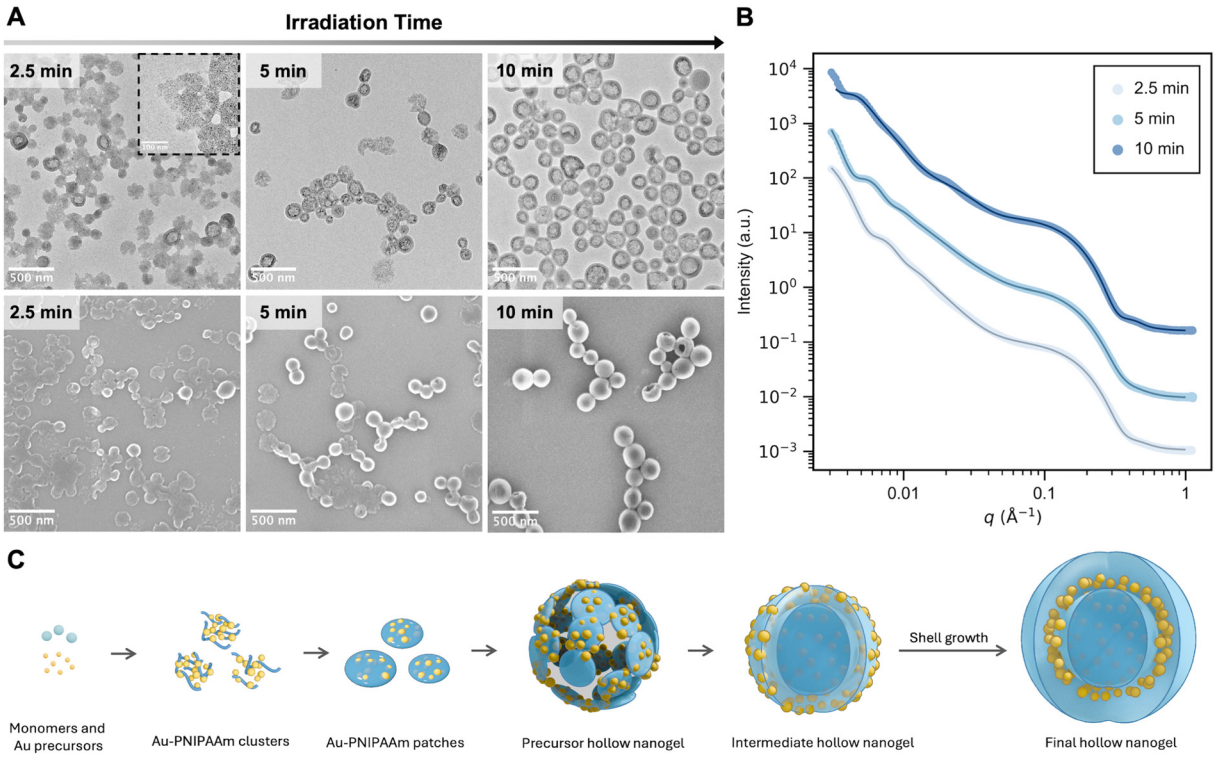

Fig. 2 Investigation of hollow nanogel formation in H40. (A) TEM (upper row) and SEM (lower row) images of H40 irradiated for 2.5, 5, and 10 minutes. (B) SAXS data of H40 at 2.5, 5, and 10 minutes fitted with a combined core–shell, sphere, and Guinier model. (C) Proposed mechanism of hollow nanogel formation.

for the excess low-q intensity arising from aggregates.[34] At 2.5 and 5 min, the Guinier contribution was pronounced, indicating the presence of large aggregates. The detailed fitting results obtained with the core–shell combination are summarized in Table S1 and Fig. 2B. The radii of AuNPs remained nearly constant at ~10–12 Å, indicating that gold reduction was largely completed in the early stage. In contrast, the core radius first increased from ~486 Å at 2.5 min to ~686 Å at 5 min, and then slightly decreased to ~637 Å at 10 min, while the shell thickness expanded markedly from ~57–75 Å at 2.5–5 min to more than 300 Å at 10 min. By 10 min, the Guinier component reflected only small aggregates, consistent with the nanogels that had stabilized due to progressive polymerization and crosslinking, which reinforced the shell and reduced large-scale clustering. Moreover, the thickened shell also facilitated local aggregation of Au nanoparticles within the shell, further contributing to structural stabilization. Attempts to fit the early scattering curves using a Guinier + sphere + sphere model, in which a simple solid-sphere function replaced the core–shell description, failed to reproduce the experimental features (Fig. S6). This result demonstrates that even at 2.5 min, the scattering already reflected a core–shell structure rather than a solid-sphere form.

Altogether, the evidence from SEM, TEM, cryo-TEM, and SAXS analyses depicts the following mechanism for the hybrid hollow nanogel formation (H40, Fig. 2C). Upon 365 nm irradiation, Au–PNIPAAm clusters formed rapidly through simultaneous reduction and precipitation polymerization, and these clusters gradually aggregated into more stable patches. At this early time point, the reduction of Au^{3+} was nearly complete, and polymerization and crosslinking dominated the subsequent process. The patches then assembled through further polymerization and inter-patch crosslinking, giving rise to precursor hollow nanogels. The presence of individual patches accounted for the surface roughness observed in the SEM images of the 2.5 min sample. As polymerization proceeded on the surface of the patch-assembled nanogels, the shell became smoother and sufficiently thick to resist collapse during SEM and TEM characterization, ultimately producing hollow nanogels with AuNPs predominantly located near the inner wall.

Based on these observations, we therefore propose that hollow nanogel formation is restricted to a specific kinetic window that requires phase separation while avoiding excessively rapid polymerization and crosslinking. Outside this window, solid nanogels are formed. Below the LCST (*e.g.*, H25), homogeneous polymerization dominates. Near the LCST at lower monomer concentrations (*e.g.*, L40), phase separation occurs, but the reduced number density of polymer nuclei favors independent cluster growth rather than aggregation into patch-like intermediates. At higher temperatures (*e.g.*, H60), rapid polymerization and crosslinking lead to the formation of a continuous polymer network with AuNPs embedded throughout the matrix.

The polydispersity index (PDI) and D_H of the hybrid nanogels were determined by DLS characterization. The sizes were 75.7, 113.2, and 164.3 nm for L25, L40, and L60, respectively, and 79.6, 238.8, and 194.0 nm for H25, H40, and H60, respectively (Fig. 3A, E, and Table 1). All samples exhibited PDIs below 0.1, confirming that nanoparticles with narrow size distributions can be successfully synthesized using this one-step approach (Fig. S7A and S7B). The sizes of the AuNPs embedded within the nanogels were further determined from TEM images, with at least 300 individual particles measured to plot size histograms (Fig. S8A, S8B, and Table 1). Most samples under different conditions showed similar AuNP sizes, ranging from 3.0 to 3.7 nm, except that H60 contained significantly larger AuNPs with an average size of 5.2 nm (Fig. 3B and F). This difference may be related to the higher initial gold precursor concentration used in the H60 sample. These results were consistent with the UV–Vis spectra. For samples synthesized under L-conditions, no significant peak shift was observed, suggesting that the AuNP size remained similar across the different synthesis temperatures (Fig. 3C). The diminished spectral feature at higher synthesis temperatures was presumably a consequence of the formation of a denser polymer network, which altered the local dielectric environment of the AuNPs (Fig. 3G). In contrast, H60 displayed a significant red-shift compared to H25 and H40, indicating the formation of larger AuNPs. Moreover, the Au weight frac-

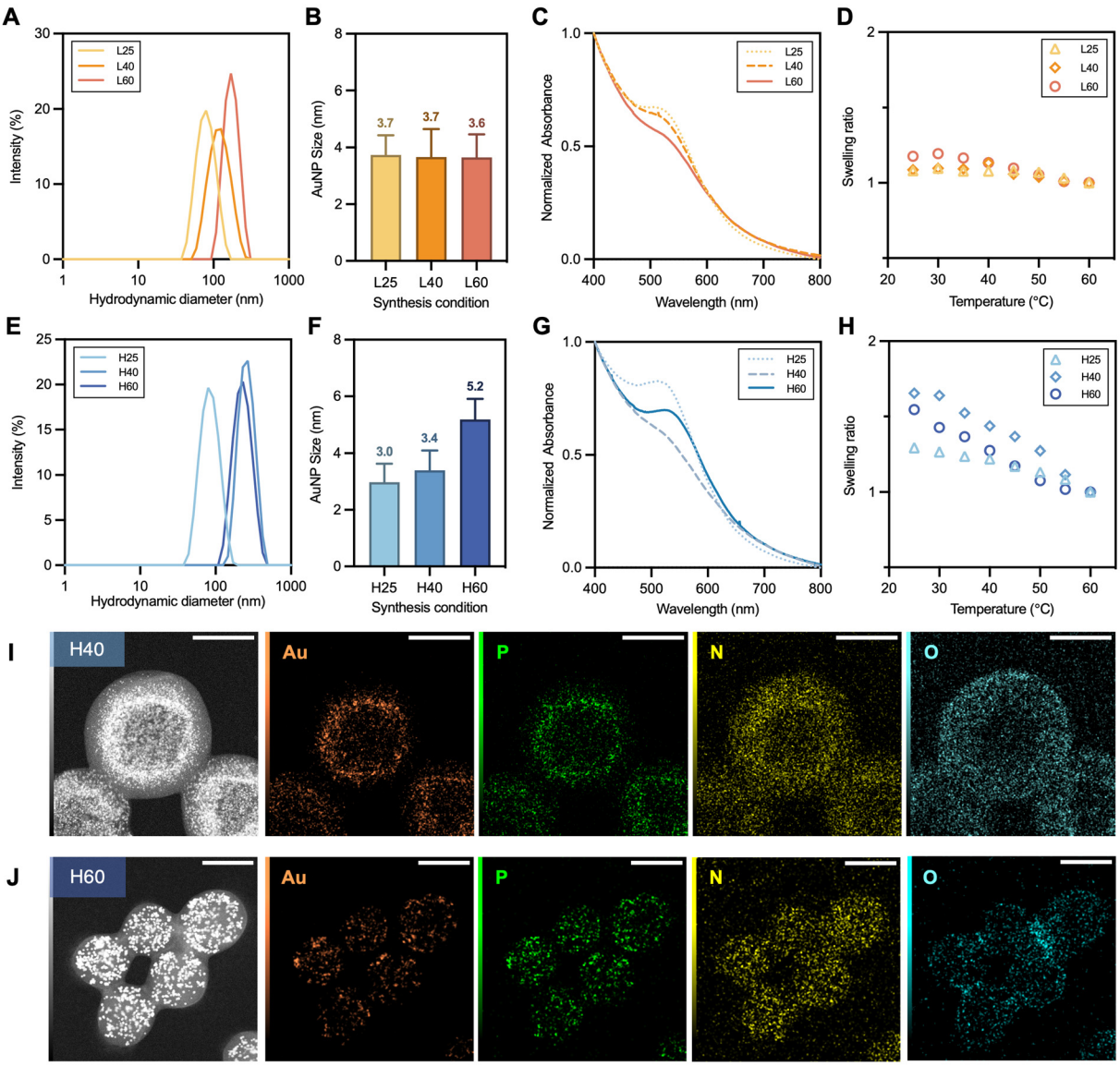

Fig. 3 Characterization of the synthesized hybrid nanogels. (A and E) Hydrodynamic diameters of L-series and H-series measured by DLS. (B and F) AuNP sizes of L-series and H-series determined from TEM images (n = 300). (C and G) UV-Vis spectra of L-series and H-series. (D and H) Temperature-dependent swelling ratios of L-series and H-series measured by DLS from 25 °C to 60 °C at 5 °C intervals. (I and J) EDS elemental maps (Au, P, N, and O) for H40 (I) and H60 (J) (scale bar = 100 nm).

tion of the hybrid nanogels was quantified by ICP-OES (Table 1). The results show that the H-series samples exhibited a higher Au content than the L-series samples. Furthermore, the H60 sample exhibited a markedly higher Au content than other samples. This trend correlates with the larger AuNP size observed in H60, which may increase the Au mass contribution within the nanogels.

Furthermore, elemental mapping using energy-dispersive X-ray spectroscopy (EDS) was performed to investigate the composition and spatial distribution of elements in the hybrid nanogels. As shown in Fig. 3I, J, S9A and S9B, the mapping of Au, N, and O confirmed that the AuNPs were embedded within the polymer network. In addition, the coexistence of P and Au was also observed. Since phosphorus originates from the photoinitiator LAP, the overlapping distributions of Au and P suggest that LAP was involved in the nucleation and stabilization of AuNPs. The metallic state (Au^0) of Au was further confirmed by Au L_3-edge X-ray absorption fine structure (XAFS) spectroscopy of H40 and H60, as the spectra exhibit features similar to those of an Au foil reference (Fig. S10).

The thermoresponsive properties of the synthesized hybrid nanogels were evaluated through measuring D_H at different temperatures using DLS. Swelling ratios were defined as the volume ratio of the D_H at a given temperature relative to the D_H at 60 °C. While the L-series exhibited almost no shrinkage upon increasing the temperature (Fig. 3D and S11A), the H-series showed a more pronounced decrease in D_H with increasing temperature (Fig. 3H and S11B). These differences in swelling ratios may arise from the variation in the ratio of the monomer to photoinitiator, which influences the polymerization kinetics and the properties of the resulting networks. With a lower monomer-to-photoinitiator ratio, more segments are formed during the initiation, leading to a suppressed average molecular weight and a higher charge density. As a result, the L-series nanogels likely formed networks with higher crosslinking density and electrostatic stabilization, which limited their thermoresponsive shrinkage. In contrast, the higher monomer-to-photoinitiator ratio in the H-series produced more loose polymer networks and lower charge density, allowing for more pronounced collapse with increasing temperature. Nevertheless, while the typical volume phase transition temperature (VPTT) has been predominantly reported as 32 °C for PNIPAAm nanogels, no clear VPTT was observed in the synthesized hybrid nanogel. Instead, the D_H decreased gradually with increasing temperature (Fig. 3H), which may be attributed to steric hindrance from the embedded AuNPs or to electrostatic repulsion arising from photoinitiator-derived fragments within the polymer networks.[35]

The catalytic activities of the synthesized Au–PNIPAAm hybrid nanogels with different structures were evaluated *via* the reduction of 4-nitrophenol (4-NP) to 4-aminophenol (4-AP). In a typical reaction, yellowish 4-NP was reduced to colorless 4-AP by excess sodium borohydride ($NaBH_4$) in the presence of hybrid nanogels as the catalyst (Fig. 4A).[36] The reduction of 4-NP has been widely used as a model reaction for demonstrating the catalytic activities of various metallic nanoparticles. It is known to follow the Langmuir–Hinshelwood model, where both reactants adsorb onto the particle surface before reaction.[37] In this study, $NaBH_4$ was employed in large excess ($NaBH_4$/4-NP = 500), allowing its concentration to be considered effectively constant during the reaction. Under these conditions, the reaction exhibits pseudo-first-order kinetics. The reaction progress was easily monitored by tracking the decrease in the absorbance peak of 4-NP at 400 nm (Fig. 4A), and the rate constants were calculated using the equation:

$$\ln\frac{A_t}{A_0} = -k_{app}t$$

To investigate the temperature-dependent catalytic activities of hybrid nanogels, non-thermoresponsive citrate-capped AuNPs were synthesized as a control. Following the Turkevich method, the citrate-capped AuNPs exhibited a characteristic absorption maximum at 519 nm (Fig. S12A) and an average size of 13.7 nm, as determined *via* TEM (Fig. S12B and S12C). As shown in the Arrhenius plot from 25 °C to 60 °C (Fig. 4B), the catalytic activity of citrate-capped AuNPs followed the standard Arrhenius behavior, with the logarithmic apparent rate constant displaying a linear relationship with $1/T$. Similarly, the reaction catalyzed by L40 showed the same linear trend as the control (Fig. 4C). In contrast, the reactions catalyzed by H40 and H60 deviated from this linear behavior, with noticeable deviations occurring at 45–55 °C and 50–55 °C, respectively (Fig. 4D and E). These differences in temperature-dependent catalytic activities can be attributed to the distinct swelling ratios. Upon heating, the nanogels deswelled, and the collapsed polymer networks hindered the diffusion and accessibility of reactants, thereby reducing the apparent kinetic constants (Fig. 4F).[38,39] Since L40 exhibited almost no deswelling with increasing temperature (Fig. 3D), its catalytic activity remained consistent with the standard Arrhenius trend observed for citrate-capped AuNPs. However, both H40 and H60 showed significantly stronger thermoresponsive behavior (Fig. 3H), thus leading to deviations from the typical linear Arrhenius relationship.

The observed deviations in catalytic activity for the reactions catalyzed by H40 and H60 suggest structural changes within the nanogels. Although DLS provided evidence of deswelling through decreases in D_H (Fig. S11A and S11B), this technique primarily reflects changes in the hydrated outer shell and cannot resolve the collapse of the polymer networks that directly affect substrate diffusion. To overcome this limitation, temperature-controlled SAXS measurements were employed as a complementary method to evaluate the thermoresponsive properties of the hybrid nanogels. As shown in Fig. 4G–I, both H40 (Fig. 4H) and H60 (Fig. 4I) exhibited pronounced changes in the low-q region at 55 °C, whereas L40 (Fig. 4G) showed no significant difference between 25 °C and 55 °C. These results are consistent with the deviations in catalytic activity, which emerged at approximately 45–55 °C, confirming that the reduced catalytic performance originates from

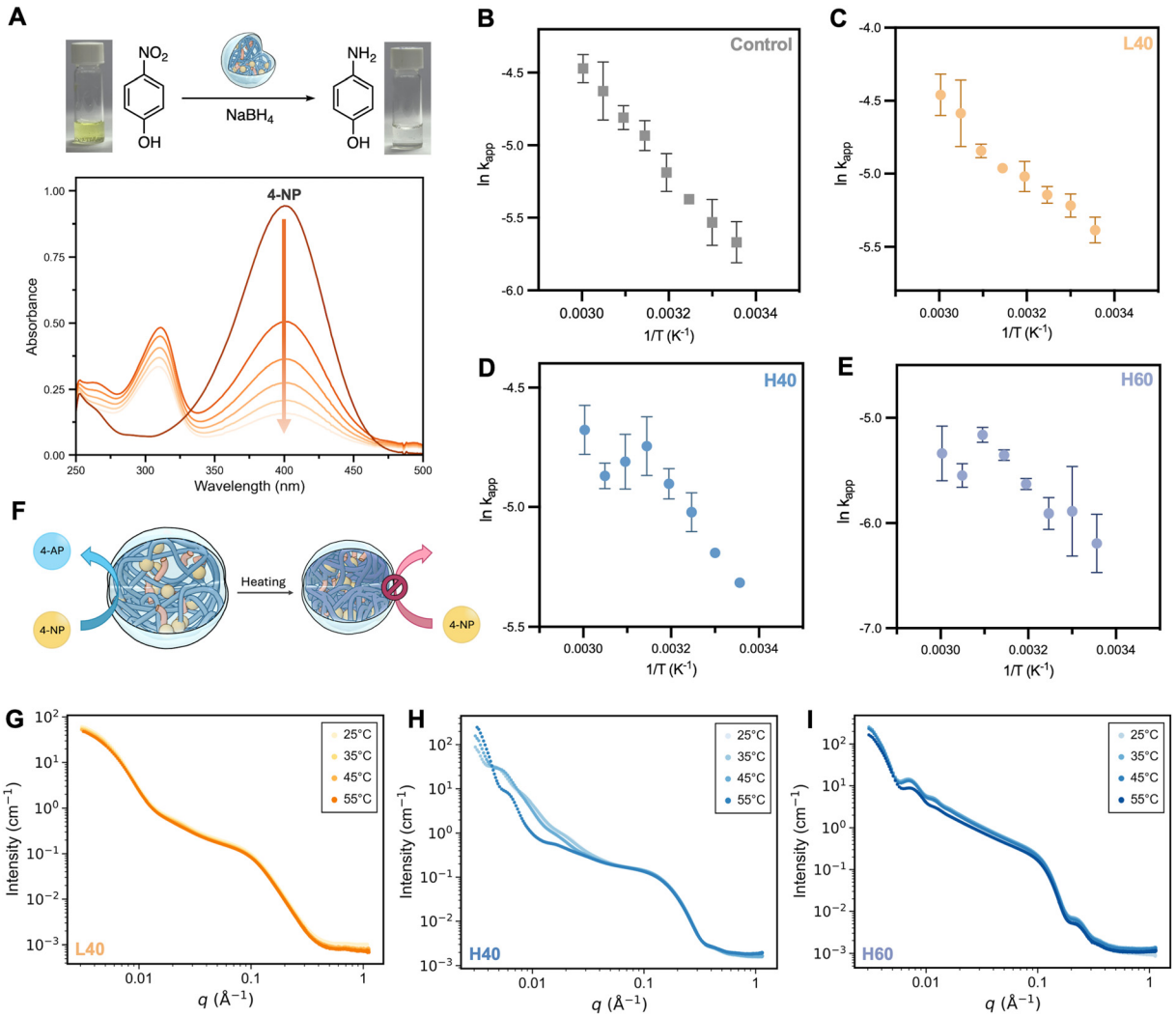

Fig. 4 Evaluation of temperature-dependent catalytic activities by 4-NP reduction. (A) Schematic of 4-NP reduction by $NaBH_4$ in the presence of hybrid nanogels, and the typical absorbance change during the reaction, where the decrease at 400 nm indicates 4-NP reduction. Arrhenius plots from 25 °C to 60 °C at 5 °C intervals for (B) citrate-capped AuNPs, (C) L40, (D) H40, and (E) H60. Error bars represent the standard deviation (n = 3). (F) Schematic of temperature-dependent catalytic activities of hybrid nanogels. SAXS data for (G) L40, (H) H40, and (I) H60 acquired from 25–55 °C in 10 °C increments.

temperature-triggered compaction of the polymer networks. Taken together, while citrate-capped AuNPs and L40 maintained standard Arrhenius behavior due to the absence of significant deswelling, both H40 and H60 exhibited thermoresponsive responses, where deswelling and network collapse restricted substrate accessibility. This correlation between the polymer architecture, thermoresponsive structural changes, and catalytic activity underlines the critical role of nanogel design in regulating reaction kinetics and highlights their potential as tunable catalytic platforms.

Conclusions

We have developed a one-step photochemical synthesis of Au–PNIPAAm nanogels *via* simultaneous reduction and polymerization, enabling the rapid formation of both solid and hollow hybrid nanogels through adjusting reaction conditions. The formation mechanism of the novel hollow nanogels was systematically investigated and proposed based on characterization using various EM characterization studies and SAXS analysis, wherein small Au–PNIPAAm patches formed in the early stage and subsequently assembled into precursor hollow nanogels, followed by further polymerization and crosslinking to yield hybrid hollow nanogels with AuNPs predominantly distributed near the inner wall. The temperature-dependent catalytic activity was evaluated through 4-NP reduction, where the collapse of the polymer network at high temperature led to reduced substrate accessibility and consequently reduced catalytic activity. These results not only demonstrate the structural tunability and functionality of the hybrid nanogels but also highlight the potential of this rapid photochemical approach

for designing responsive nanomaterials with distinct morphologies and catalytic properties.

Experimental

Chemicals and materials

Tetrachloroauric(III) acid trihydrate ($HAuCl_4 \cdot 3H_2O$) and trisodium citrate dihydrate were purchased from Thermo Scientific. *N*-Isopropylacrylamide (97%, NIPAAm), *N*,*N*′-methylenebis (acrylamide) (99%, BIS), lithium phenyl-2,4,6-trimethylbenzoylphosphinate (≥95%, LAP), 4-nitrophenol (≥99%, 4-NP), and sodium borohydride (98%, $NaBH_4$) were purchased from Sigma-Aldrich and used as received. Glassware was cleaned with aqua regia and rinsed with DI water.

Synthesis of Au–PNIPAAm hybrid nanogels

Au–PNIPAAm hybrid nanogels were synthesized *via* a single-step approach in which polymerization and reduction occurred simultaneously. Stock solutions of NIPAAm (1 M), BIS (100 mM), LAP (25 mg mL^{-1}), and $HAuCl_4$ (50 mM) were prepared in DI water prior to synthesis. For a typical synthesis, appropriate volumes of NIPAAm, BIS, and LAP stock solutions were mixed in a 100 mL round-bottom flask, and the total volume was adjusted to 18 mL with DI water to achieve the desired concentrations. The solution was placed in a water bath at the desired temperature and purged with N_2 gas for 20 minutes. Subsequently, 2 mL of $HAuCl_4$ solution (prepared by diluting the 50 mM stock solution to the desired concentration without prior N_2 purging) was injected into the flask while maintaining an N_2 atmosphere. The mixture was irradiated with 365 nm UV light for 10 minutes. After irradiation, the solution was cooled in an ice bath and purged with O_2 gas to quench the radical reaction. Finally, the produced Au–PNIPAAm hybrid nanogels were purified by centrifugation twice at 25 °C to remove the unreacted reagents in the supernatant.

Synthesis of citrate-capped AuNPs

Citrate-stabilized AuNPs were synthesized using a modified Turkevich method. A solution of $HAuCl_4$ (1 mM, 50 mL) was heated to boiling under reflux, and trisodium citrate dihydrate (38.8 mM, 5 mL) was rapidly added. The reaction mixture was maintained at reflux for an additional 10 minutes until a deep red color developed, indicating nanoparticle formation.

Characterization

Dynamic light scattering (DLS). The hydrodynamic diameter and polydispersity index (PDI) were measured using a dynamic light scattering analyzer (Zetasizer Ultra, Malvern). Measurements were conducted at a fixed backscattering angle of 173° after equilibrating the samples for 5 min at the desired temperatures.

UV-Vis spectroscopy. The absorption spectra were acquired using a UV-Vis spectrophotometer (SpectraMax ABS Plus) at room temperature.

Scanning electron microscopy (SEM). SEM (ULTRA PLUS) was performed at an accelerating voltage of 15 kV using a secondary electron detector. Samples were prepared by depositing a drop of diluted aqueous solution onto a silicon wafer, drying under vacuum at room temperature, and sputter-coating with platinum prior to imaging.

Transmission electron microscopy (TEM) and cryogenic transmission electron microscopy (cryo-TEM). TEM (JEOL JEM-ARM300F2) was operated at 300 kV and equipped with a Gatan 1k CCD camera. Samples were prepared by dropping a diluted aqueous solution onto a carbon-coated copper grid and drying under vacuum at room temperature. Cryo-TEM (FEI Tecnai G2 F20 TWIN) was operated at 200 kV and equipped with Gatan 4k × 4k CCD and DE20 cameras. Samples were vitrified on holey carbon TEM grids using an FEI Vitrobot.

Small- and wide-angle X-ray scattering (SAXS/WAXS). SAXS/WAXS experiments were carried out at beamline TPS 13A (NSRRC, Taiwan).[40,41] Samples were loaded into a sealed liquid cell (X-ray path length ≈ 2.0 mm) equipped with polyimide Kapton windows and O-ring gaskets. Data collection was performed with an incident X-ray energy of 15 keV. Each specimen was exposed for 10 s in a single frame to monitor radiation sensitivity. In temperature-controlled measurements, the liquid cell was equilibrated at the desired temperature for at least 10 minutes before data collection. For background correction, scattering profiles from air and matched buffer were recorded with single 20 s exposures. The SAXS patterns were collected on an Eiger X 9 M detector positioned at 5 m, covering a momentum transfer range of 0.003–0.34 $Å^{-1}$, while the WAXS data were simultaneously acquired with an Eiger X 1 M detector at 0.652 m (q = 0.14–1 $Å^{-1}$). The raw images were normalized and subtracted using TPS13A reduction software (version 4.89).[40] Subsequently, one-dimensional scattering curves from the two detectors were merged with PRIMUS (ATSAS package)[42] to obtain a continuous q-range. Structural modeling of the samples was carried out using SasView (v6.1.0) (https://www.sasview.org/), with a custom model combining the core–shell, sphere, and Guinier functions.

X-ray absorption fine structure (XAFS). The Au L_3-edge XAFS spectra of H40 and H60 were collected at beamline TPS 44A (NSRRC, Taiwan). All measurements were carried out in transmission mode, with Au metal foil measured simultaneously for calibration of the incident X-ray photon energy. The acquired data were processed using standard procedures implemented in the Demeter software package.

Inductively coupled plasma optical emission spectroscopy (ICP-OES). The Au content in the hybrid nanogels was determined using an ICP-OES instrument (Agilent 5800 ICP-OES). The samples were digested with aqua regia and filtered prior to analysis.

Evaluation of catalytic activity *via* 4-nitrophenol reduction

The catalytic activities of the synthesized hybrid nanogels were evaluated *via* the reduction of 4-nitrophenol (4-NP) to 4-aminophenol (4-AP) at varying temperatures. In a typical reaction, 750 μL of 100 mM $NaBH_4$ was added to 2000 μL of deionized

water in a cuvette, followed by the addition of 150 μL of 1 mM 4-NP solution. The solution and the Au–PNIPAAm hybrid nanogel catalyst (0.05 mg mL^{-1}) were equilibrated separately at the target temperature for at least 10 minutes. Subsequently, 100 μL of the catalyst suspension was added to the mixture to initiate the reaction. UV-vis absorption spectra in the range of 190–1100 nm were recorded every 1 minute using a UV-Vis spectrophotometer (Agilent 8453) equipped with a temperature-controlled module. The reduction progress was monitored by tracking the decrease in the absorbance peak of 4-NP at 400 nm. The apparent rate constants (k_{app}) were determined from the slope of the linear plot of $\ln(A_t/A_0)$ *versus* time, according to the equation:

$$\ln\frac{A_t}{A_0} = -k_{app}t.$$

Author contributions

The manuscript was written through the contributions of all authors. All authors have given approval to the final version of the manuscript.

Conflicts of interest

There are no conflicts to declare.

Data availability

The data supporting this article have been included as part of the supplementary information (SI). Supplementary information: SEM images, photographs and UV–Vis spectra of samples at different irradiation times, cryo-TEM images, additional DLS data, EDS analysis, characterization of citrate-capped AuNPs, XAFS data, and detailed SAXS model-fitting results (Table S1). See DOI: https://doi.org/10.1039/d5nr04546k.

Acknowledgements

We are thankful for the funding support from the National Science and Technology Council (former Ministry of Science and Technology) in Taiwan: NSTC 112-2628-M-001-004-MY3 and NSTC 114-2113-M-001-018-, and Academia Sinica: AS-GC-111-M03 and AS-iMATE-113-21. Technical support from the Advanced Materials Characterization Lab, Institute of Atomic & Molecular Sciences (IAMS), Academia Sinica, is gratefully acknowledged. The cryo-EM experiments were performed at the Academia Sinica Cryo-EM Facility (ASCEM). ASCEM is supported by the Academia Sinica Core Facility and Innovative Instrument Project (Grant No. AS-CFII-111-210). We thank Ms. Mei-Ying Chung for assistance with ICP-OES analyses. We also thank Dr Chen-Hsiung Hung and Kai-Chun Hsu for their assistance with the UV-Vis spectrophotometer (Agilent 8453) equipped with a temperature-controlled module.

References

1 X. Liu, Y. Yang and M. W. Urban, *Macromol. Rapid Commun.*, 2017, **38**, 1700030.
2 M. Fatima, W. H. Almalki, T. Khan, A. Sahebkar and P. Kesharwani, *Adv. Mater.*, 2024, **36**, 2312939.
3 T. Shu, Q. Shen, X. Zhang and M. J. Serpe, *Analyst*, 2020, **145**, 5713–5724.
4 H. Jia, J. Cao and Y. Lu, *Curr. Opin. Green Sustain. Chem.*, 2017, **4**, 16–22.
5 J. Zheng, X. Cheng, H. Zhang, X. Bai, R. Ai, L. Shao and J. Wang, *Chem. Rev.*, 2021, **121**, 13342–13453.
6 Y. Hang, A. Wang and N. Wu, *Chem. Soc. Rev.*, 2024, **53**, 2932–2971.
7 Z. Ye, C. Chen, L. Cao, Z. Cai, C. Xu, H.-I. Kim, J. P. Giraldo, A. G. Kanaras and Y. Yin, *Angew. Chem., Int. Ed.*, 2024, **63**, e202408020.
8 M. Yon, B. Lonetti, S. Gineste, J. Perez, D. Goudouneche, L. Weingarten, J.-D. Marty and D. Ciuculescu-Pradines, *J. Colloid Interface Sci.*, 2025, **679**, 9–19.
9 Y.-S. Chen, S. J. Yoon, W. Frey, M. Dockery and S. Emelianov, *Nat. Commun.*, 2017, **8**, 15782.
10 T. Ding and J. J. Baumberg, *Nanoscale Adv.*, 2020, **2**, 1410–1416.
11 Y.-X. Wang, Y. Li, S.-H. Qiao, J. Kang, Z.-L. Shen, N.-N. Zhang, Z. An, X. Wang and K. Liu, *J. Phys. Chem. Lett.*, 2021, **12**, 4713–4721.
12 S. Wu, L. Lei, Y. Xia, S. Oliver, X. Chen, C. Boyer, Z. Nie and S. Shi, *Polym. Chem.*, 2021, **12**, 6903–6913.
13 B. P. Nayak, H. J. Kim, S. Nayak, W. Wang, W. Bu, S. K. Mallapragada and D. Vaknin, *ACS Macro Lett.*, 2023, **12**, 1659–1664.
14 P. Pongsanon, Y. Oota, A. Kawamura, H. Kawasaki and T. Miyata, *Macromolecules*, 2023, **56**, 9853–9865.
15 H. Sun and J. Du, *Nanoscale*, 2018, **10**, 17354–17361.
16 P. N. Eyimegwu, J. A. Lartey and J.-H. Kim, *ACS Appl. Nano Mater.*, 2019, **2**, 6057–6066.
17 D. J. Kim, J. Yoon, D.-H. Kim, S.-G. Park and S.-H. Kim, *ACS Appl. Mater. Interfaces*, 2020, **12**, 48188–48197.
18 S. Lee, S. Kim, D. Kim, J. S. Kim, H. Kim, J. Park, J. Song and I. Choi, *J. Nanobiotechnol.*, 2023, **21**, 191.
19 D. Kim, S. Lee, D. Shin, S. Hong, S. Park, J. Choe, J. Seo, J. B. Lee and I. Choi, *ACS Mater. Lett.*, 2024, **6**, 409–417.
20 J. Dubbert, K. Nothdurft, M. Karg and W. Richtering, *Macromol. Rapid Commun.*, 2015, **36**, 159–164.
21 X. Wang, J. Feng, Y. Bai, Q. Zhang and Y. Yin, *Chem. Rev.*, 2016, **116**, 10983–11060.
22 H. Xie, S. Zhu, J. Cao, J. Lee, Y. Yin, D. Zhou, J. Yan, H.-H. Jeong, T.-C. Lee, Y. Zhang, Q. Pu and Y. Lan, *Chem. Eng. J.*, 2025, **511**, 161872.
23 G. Kim, K. Park, Z. Zheng and S. Jin, *Langmuir*, 2020, **36**, 6202–6209.
24 G. Kim, K. Park, Z. Zheng, S. Choi and S. Jin, *J. Phys. Chem. B*, 2020, **124**, 10276–10281.

25 W. Wichaita, D. Polpanich and P. Tangboriboonrat, *Ind. Eng. Chem. Res.*, 2019, **58**, 20880–20901.
26 B. D. Fairbanks, M. P. Schwartz, C. N. Bowman and K. S. Anseth, *Biomaterials*, 2009, **30**, 6702–6707.
27 P. Bianchi, G. Petit and J.-C. M. Monbaliu, *React. Chem. Eng.*, 2020, **5**, 1224–1236.
28 P. Kunwar, A. V. S. Jannini, Z. Xiong, M. J. Ransbottom, J. S. Perkins, J. H. Henderson, J. M. Hasenwinkel and P. Soman, *ACS Appl. Mater. Interfaces*, 2020, **12**, 1640–1649.
29 J. Wu, Z. Wu, H. Zeng, D. Liu, Z. Ji, X. Xu, X. Jia, P. Jiang, Z. Fan, X. Wang and F. Zhou, *Chem. Mater.*, 2022, **34**, 6129–6141.
30 R. Pelton, *Adv. Colloid Interface Sci.*, 2000, **85**, 1–33.
31 J. C. Foster, I. Akar, M. C. Grocott, A. K. Pearce, R. T. Mathers and R. K. O'Reilly, *ACS Macro Lett.*, 2020, **9**, 1700–1707.
32 A. Vdovchenko, A. K. Pearce, M. Freeley, R. K. O'Reilly and M. Resmini, *Polym. Chem.*, 2021, **12**, 6854–6864.
33 O. L. J. Virtanen and W. Richtering, *Colloid Polym. Sci.*, 2014, **292**, 1743–1756.
34 D. Lombardo, G. Munaò, P. Calandra, L. Pasqua and M. T. Caccamo, *Phys. Chem. Chem. Phys.*, 2019, **21**, 11983–11991.
35 J. Rubio-Retama, N. E. Zafeiropoulos, C. Serafinelli, R. Rojas-Reyna, B. Voit, E. Lopez Cabarcos and M. Stamm, *Langmuir*, 2007, **23**, 10280–10285.
36 P. Zhao, X. Feng, D. Huang, G. Yang and D. Astruc, *Coord. Chem. Rev.*, 2015, **287**, 114–136.
37 S. Wunder, F. Polzer, Y. Lu, Y. Mei and M. Ballauff, *J. Phys. Chem. C*, 2010, **114**, 8814–8820.
38 T. Brändel, V. Sabadasch, Y. Hannappel and T. Hellweg, *ACS Omega*, 2019, **4**, 4636–4649.
39 Y. Chen, Z. Wang, Y. W. Harn, S. Pan, Z. Li, S. Lin, J. Peng, G. Zhang and Z. Lin, *Angew. Chem., Int. Ed.*, 2019, **58**, 11910–11917.
40 O. Shih, K.-F. Liao, Y.-Q. Yeh, C.-J. Su, C.-A. Wang, J.-W. Chang, W.-R. Wu, C.-C. Liang, C.-Y. Lin, T.-H. Lee, C.-H. Chang, L.-C. Chiang, C.-F. Chang, D.-G. Liu, M.-H. Lee, C.-Y. Liu, T.-W. Hsu, B. Mansel, M.-C. Ho, C.-Y. Shu, F. Lee, E. Yen, T.-C. Lin and U. Jeng, *J. Appl. Crystallogr.*, 2022, **55**, 340–352.
41 D.-G. Liu, C.-H. Chang, L.-C. Chiang, M.-H. Lee, C.-F. Chang, C.-Y. Lin, C.-C. Liang, T.-H. Lee, S.-W. Lin, C.-Y. Liu, C.-S. Hwang, J.-C. Huang, C.-K. Kuan, H.-S. Wang, Y.-C. Liu, F.-H. Tseng, J.-Y. Chuang, W.-R. Liao, H.-C. Li, C.-J. Su, K.-F. Liao, Y.-Q. Yeh, O. Shih, W.-R. Wu, C.-A. Wang and U. Jeng, *J. Synchrotron Radiat.*, 2021, **28**, 1954–1965.
42 K. Manalastas-Cantos, P. V. Konarev, N. R. Hajizadeh, A. G. Kikhney, M. V. Petoukhov, D. S. Molodenskiy, A. Panjkovich, H. D. T. Mertens, A. Gruzinov, C. Borges, C. M. Jeffries, D. I. Svergun and D. Franke, *J. Appl. Crystallogr.*, 2021, **54**, 343–355.